Energy & Environmental Science

Accepted Manuscript

ROYAL SOCIETY OF CHEMISTRY

www.rsc.org/ees

Cite this: DOI: 10.1039/c0xx00000x

www.rsc.org/xxxxxx

ARTICLE TYPE

Metal-Organic Framework Route to In-Situ Encapsulation of Co@Co_3O_4@C Core@Bishell Nanoparticles into Highly Ordered Porous Carbon Matrix for Oxygen Reduction

Wei Xia,[a] Ruqiang Zou,*[a] Li An,[a] Dingguo Xia[a] and Shaojun Guo*[b]

Received (in XXX, XXX) XthXXXXXXXXX 20XX, Accepted Xth XXXXXXXXX 20XX
DOI: 10.1039/b000000x

Rational design of non-noble metal catalysts with the electrocatalytic activity comparable or even superior to Pt is extremely important for the future fuel cell-based renewable energy device. Herein, we demonstrate a new concept that metal-organic framework (MOF) can be used as a novel precursor to in-situ encapsulate Co@Co_3O_4@C core@bishell nanoparticles (NPs) into a highly ordered porous carbon matrix (CM) (denoted as Co@Co_3O_4@C-CM). The central cobalt ions from MOF are used as metal source to produce Co metal cores, which are later transformed into fancy Co@Co_3O_4 nanostructure via a controlled oxidation. The most notable feature of our Co@Co_3O_4@C-CM is that the highly ordered CM can provide much better transport pathway than the disordered pure MOF derived nanostructure that can facilitate the mass transport of O_2 and electrolyte. As a result, the well-designed Co@Co_3O_4@C-CM derived from MOF shows almost identical activity but superior stability and methanol tolerance for ORR relatively to the commercial Pt/C in alkaline medium. Our work first reports the novel Co@Co_3O_4@C nanostructure from MOF and also reveals the important role of the introduction of highly ordered carbon matrix into MOF derived catalyst on enhancing the ORR activity and stability. To the best of our knowledge, Co@Co_3O_4@C-CM is the most efficient non-noble metal nanocatalyst ever reported for ORR.

Introduction

The oxygen reduction reaction (ORR) has been one of the most fundamentally and technologically important electrochemical reactions for fuel cells and lithium air batteries.[1-3] To date, Pt-based nanomaterials are still the dominant and best electrocatalysts for promoting ORR. However, the scarcity, high cost and low stability of Pt hinter its practical application in fuel cell device. To solve these bottlenecks, non-platinum-group-metal (non-PGM) electrocatalysts as alternatives to Pt for ORR have been intensively pursued.[4-8] One of the major advances is the development of metal-nitrogen-carbon (M-N-C) catalysts from Fe-N_4 or Co-N_4 macrocycle precursors.[9] Metal-organic frameworks (MOFs), built from the combination of metal ions and organic linkers,[10-12] possess the particular porous structures, which could be tailored with rich Fe-N_4 or Co-N_4 coordinate moieties. After the carbonization under inert atmosphere, it endows the potential abundant M-N-C active sites in the MOF-derived catalysts. Furthermore, the inherent high surface area of MOF-derived porous carbon materials is another advantage as electrochemical catalysts.[13-16] These interesting properties of MOF materials have recently stimulated the researchers to develop their applications as active ORR catalysts.[17-20] Up to now, the existed MOF-derived catalysts still have much higher overpotential for ORR than Pt because of two key aspects. One is related to the chemical composition. Most of the MOF-derived ORR catalysts are focused on either nitrogen-doped carbon or M-N-C structure, which exhibit valid active sites for ORR catalysis but not very effective. The other is the lack of enough effective space for the diffusion of O_2 and electrolyte onto catalysts. In this regard, rapid mass transport property of ordered carbon nanomaterials has become a key factor in pursuing more efficient ORR catalysts.[18,21] Though traditional MOFs have the inherent advantage in creating porous catalysts with high surface areas, the pore structures of the derived catalysts are usually destroyed after the carbonization process, only resulting in disordered and non-interconnected pore structure that is not beneficial for mass transport in the catalyst. Therefore, rational design of MOF-derived nanocatalysts with the ideal three-dimensional interconnected highly ordered pores, in which O_2 and H_2O are free to go through at each dimension, is highly desirable yet a great challenge to date.

Herein, we report a novel MOF induced strategy to prepare new Co@Co_3O_4@C core@bishell nanoparticles (NPs) *in-situ* encapsulated into highly ordered porous carbon matrix (CM) (denoted as Co@Co_3O_4@C-CM), which is very different from the preparation of traditional nanocatalysts directly derived from MOFs. The central cobalt ions from MOFs were used as metal source to produce Co metal cores, which were later transformed into Co@Co_3O_4 NPs via a simple oxidation process. Co_3O_4 has

proved to be ORR active but suffers from low electrical conductivity and low stability.[22,23] Here, the organic ligands from MOFs were transformed into porous graphitic carbon, which could *in-situ* wrap the metal oxide NPs, resulting in the fancy $Co@Co_3O_4@C$ core@bishell nanostructure. This can create a very strong interaction/contact between the metal oxide and carbon shell linked to CM, which is very important for not only enhancing the electron transfer between NPs and porous CM (enhancing the ORR activity), but also making the NPs hard to detach from the CM support (enhancing the ORR stability). Mostly important, $Co@Co_3O_4@C$-CM has much better transport pathway for oxygen and electrolyte than catalysts prepared from pure MOF crystals ($Co@Co_3O_4$-C) (**Fig. 1**), which makes the new catalyst have much better ORR activity than $Co@Co_3O_4$-C, and almost identical activity but superior stability relative to Pt/C catalyst.

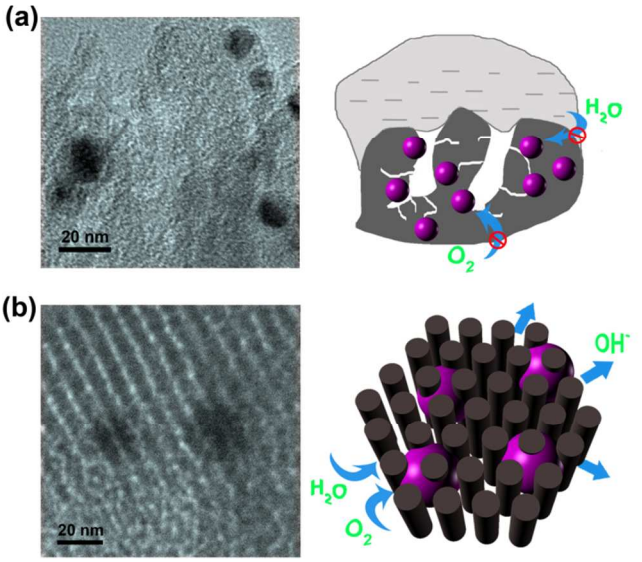

Fig. 1 The concept on the design of (a) $Co@Co_3O_4$-C and (b) $Co@Co_3O_4@C$-CM for promoting ORR.

Experimental Section

Catalysts preparation

Synthesis of MOF. MOF was prepared as described previously with some modification.[24] $Co(NO_3)_2{\cdot}6H_2O$ (0.840 g, 2.88 mmol) and benzimidazole (0.682 g, 5.76 mmol) were dissolved in 72 mL of N,N′-dimethylformamide (DMF) in a 100 mL glass vial. The vessel was sealed and heated up to 130 °C at a heating rate of 5 °C min^{-1}. It was kept at 130 °C for 48 h and then cooled down to room temperature slowly (0.4 °C min^{-1}). The purple crystals were filtered out and washed with ethanol for 3 times, and finally dried under vacuum at 100 °C for 8 h.

Synthesis of MOF-CM. Carbon support CM was first prepared according to the reported procedure [25] and then treated with concentrated nitric acid at 80 °C to increase the carboxyl group on the surface. For the preparation of MOF-CM composite, $Co(NO_3)_2{\cdot}6H_2O$ (0.210 g, 0.72 mmol) was dissolved with DMF (20 mL) in a 100 mL glass vial. The above modified CM (0.050 g) was added to the stock solution and sonicated for 5 min. After another stirring for 10 min, a solution containing benzimidazole (0.170 g, 1.44 mmol) and DMF (52 mL) was added and the mixture was stirred for 10 min. The vessel was sealed and heated up to 130 °C with a heating rate of 5 °C min^{-1}. It was kept at 130 °C for 48 h and then cooled down to room temperature slowly (0.4 °C min^{-1}). The as-formed MOF-CM composite was collected by centrifugation and washed with ethanol for three times. During centrifugation, the desired composite was separated from the pure MOF crystals by the different densities. The product was finally dried under vacuum at 100 °C for 8 h.

Synthesis of $Co@Co_3O_4$-C and $Co@Co_3O_4@C$-CM. The above prepared MOF and MOF-CM composite were pyrolyzed at 700 °C for 2 h under Ar atmosphere before cooling down to room temperature. Then, they were heated in an oven at 90 °C for 48 h and cooled down to room temperature naturally.

Synthesis of $Co_3O_4@C$-CM. The as-prepared $Co@Co_3O_4@C$-CM sample was further oxidized into $Co_3O_4@C$-CM after heating at 150 °C in air for 96 h.

Synthesis of $Co@Co_3O_4$-CM. $Co@Co_3O_4$ NPs loaded on CM were prepared via a conventional wet-impregnation method. 0.050 g of nitric acid treated CM was added into 50 mL of 20 wt% ethanol (ethanol/water mixed solution) containing 0.210 g of $Co(NO_3)_2{\cdot}6H_2O$. The resulting solution was sonicated and stirred for 1 h, respectively. After that, the solvent was vaporized at 80 °C under stirring and the obtained powder was further dried in an oven at 120 °C. Then, the mixture of $Co(NO_3)_2$ and CM was heat-treated at 500 °C under H_2/Ar flow (5% H_2) to reduce the Co cation and simultaneously remove the nitrate ion, followed by a mild heating process in air at 90 °C to convert the surface layer of Co into Co_3O_4.

Materials Characterization

Powder X-ray diffraction (PXRD) patterns were recorded on a Bruker D8 Advanced diffractometer using Cu Kα radiation (λ = 1.5406 Å). Nitrogen sorption isotherms were measured using a Quantachrome Autosorb-IQ instrument at 77 K. Pore size distributions (PSDs) were calculated from Quenched Solid Density Functional Theory (QSDFT) using the adsorption branch. To exclude the effects from different models in PSD, a slit/cylinder/sphere pores model was used in all cases (AsiQwin software for Quantachrome Instruments, version 2.0). Scanning electron microscopy (SEM) and Transmission electron microscopy (TEM) images were taken from Hitachi S-4800 microscope and FEI Tecnai T20, respectively. High resolution TEM (HRTEM) images were taken from FEI Tecnai F20 microscope. Elemental mapping was obtained from Bruker Quantax energy dispersive X-ray spectrometer (EDS) attached to the SEM. X-ray photoelectron spectroscopy (XPS) was performed on an Axis Ultra imaging photoelectron spectrometer with monochromatic Al Kα line. Thermogravimetric analyses (TGA) were performed on SDT Q600 analyzer (TA Instruments).

Electrochemical Measurements

The electrochemical measurements were performed on a BioLogic SP 240 electrochemical workstation using a standard three-electrode system. The catalyst coated glassy carbon rotating disk electrode (diameter 5 mm) was used as working electrode. A glassy carbon film and Ag/AgCl electrode with saturated KCl solution were applied as counter and reference electrodes, respectively. All potentials here are converted to a reversible

hydrogen electrode (RHE) scale. To prepare the working electrode, 2 mg of as-prepared electrocatalyst or Pt/C (20 wt% Pt on Vulcan XC-72) was dispersed in 2 mL of ethanol under sonication to form a homogeneous ink. Then, 20 μL of the suspension and 5 μL of 0.1 wt% Nafion solution were casted onto the GC electrode in sequence and dried in air. The loading amount of the catalysts is 0.1 mg cm^{-2}.

Cyclic voltammetry (CV) and polarization tests were performed in a N_2 and O_2-saturated 0.1 M KOH in the potential range of 0-1.2 V (vs. RHE). All the electrochemical measurements were carried out at room temperature. The electron transfer numbers during the oxygen reduction reaction were determined from the Koutechy-Levich equation.

$$\frac{1}{J} = \frac{1}{J_L} + \frac{1}{J_K} = \frac{1}{B\omega^{1/2}} + \frac{1}{J_K}$$

$$B = 0.62nFC_0(D_0)^{2/3}\upsilon^{-1/6}$$

$$J_K = nFkC_0$$

here J represents the measured current density, J_L and J_K are the diffusion- and kinetic limiting current densities, ω is the angular velocity, n is electron transfer number, F is the Faraday constant (96485 C mol^{-1}), C_o is the O_2 bulk concentration (1.26×10^{-6} mol cm^{-3}), D_o is the O_2 diffusion coefficient in the electrolyte (1.9×10^{-5} cm^2 s^{-1}) and υ is the kinetic viscosity of 0.1 mol L^{-1} KOH (0.01 cm^2 s^{-1}).

Rotating ring-disk electrode (RRDE) test was performed on a CHI 760D workstation and a MSRX electrode rotator (Pine Instrument). The electron transfer number can be obtained from the RRDE curve using the following equation:

$$n = \frac{4I_d}{I_d + {I_r}/{N}}$$

here I_d and I_r are the disk current and ring current, respectively, and N is the current collection efficiency of Pt ring (0.37).

Results and Discussion

Our synthetic route for Co@Co_3O_4@C-CM based on MOF concept is illustrated in **Fig. 2**. First, CM with hexagonally ordered mesopores was synthesized[25] and then functionalized with carboxyl groups,[26] which were allowed to coordinate with metal ions, and initiate MOF crystal growth after the addition of MOF precursors.[27,28] Notably, the highly ordered CM we use here is robust, and can not be destroyed even after high-temperature carbonization process. Then, MOF constructed from cobalt center and benzimidazole ligand[24] was introduced into the confined space of highly ordered CM. The as-prepared MOF-CM composite was pyrolyzed in an inert atmosphere to get Co@C-CM. It should be noted that Co complex could be easily decomposed and the Co^{2+} ions segregated from the MOF framework during the initial pyrolyzing stage, and then agglomerated to form the ultra-fine cobalt NPs[17] on carbon rods in highly ordered porous CM. As the heat treatment proceeded, these NPs aggregated to form larger Co@C NPs to decrease surface energy (**Fig. S1**). These Co NPs supported onto CM were highly active and their surface layers were then oxidized into Co_3O_4 by controlled heating in air, thus forming the core@bishell Co@Co_3O_4@C NPs on porous CM. The as-formed oxidized outer layers could prevent the Co core from further oxidation.[29] It should be noted that from the Co-O phase diagram, the stable phase is Co_3O_4 at elevated temperatures.[30,31] Taking this point into consideration, the Co@Co_3O_4 NPs were also fully oxidized into Co_3O_4 *via* heating the composite at 150 °C in air for 96 h, resulting in Co_3O_4@C-CM. Moreover, Co@Co_3O_4-C was also synthesized by heating pure MOF crystal under Ar flow and further oxidizing the obtained Co-C in air. These two catalysts were used as controls to demonstrate the obvious advantage of Co@Co_3O_4@C-CM for ORR.

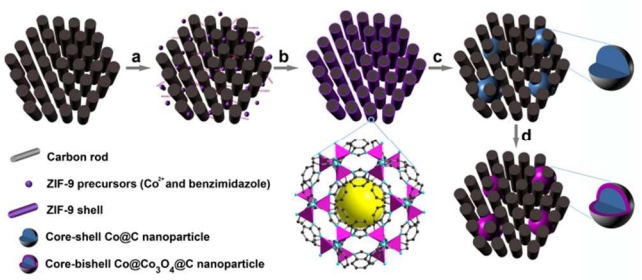

Fig. 2 Schematic illustration on the synthesis of Co@Co_3O_4@C-CM: (a) Functionalization of the CM with carboxylate groups, (b) growth of MOF on CM, (c) heat treatment under Ar flow and (d) oxidation in air at 90 °C.

The as-prepared pure MOF and CM have the purple (**Fig. S2a,c)** and black color (**Fig. S2b,d)**, respectively, while the MOF-CM composite displays a different dark purple color **(Fig. 3a)**. PXRD analysis of MOF-CM indicates well-resolved peaks that match well with that of MOF crystal (**Fig. S3**). TEM image of MOF-CM shows that CM is covered by MOF layers (**Fig. S4**). Elemental mapping of the MOF-CM composite clearly identifies the full and uniform distribution of nitrogen and carbon (**Fig. 3c**), which are the elementary substances for MOF. Furthermore, the MOF-CM composite shows rather thermal stability, similar to that of pure MOF (**Fig. S5**). These results indicate that our method is effective on the formation of MOF-CM. Then, the as-prepared stable MOF-CM composite was transformed into Co@Co_3O_4@C-CM under the sequential Ar and air annealing treatments.

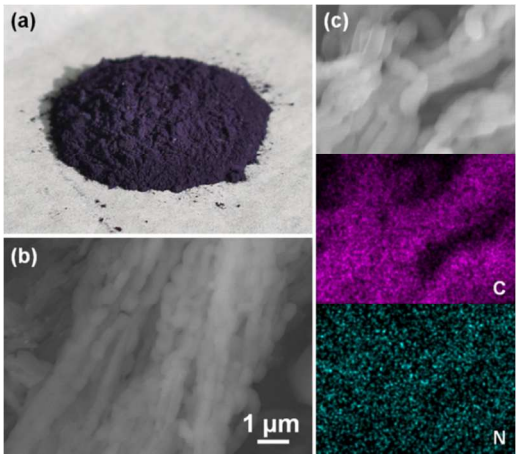

Fig. 3 View of (a) photographs, (b) SEM image and (c) EDS elemental mapping images of the MOF-CM composite.

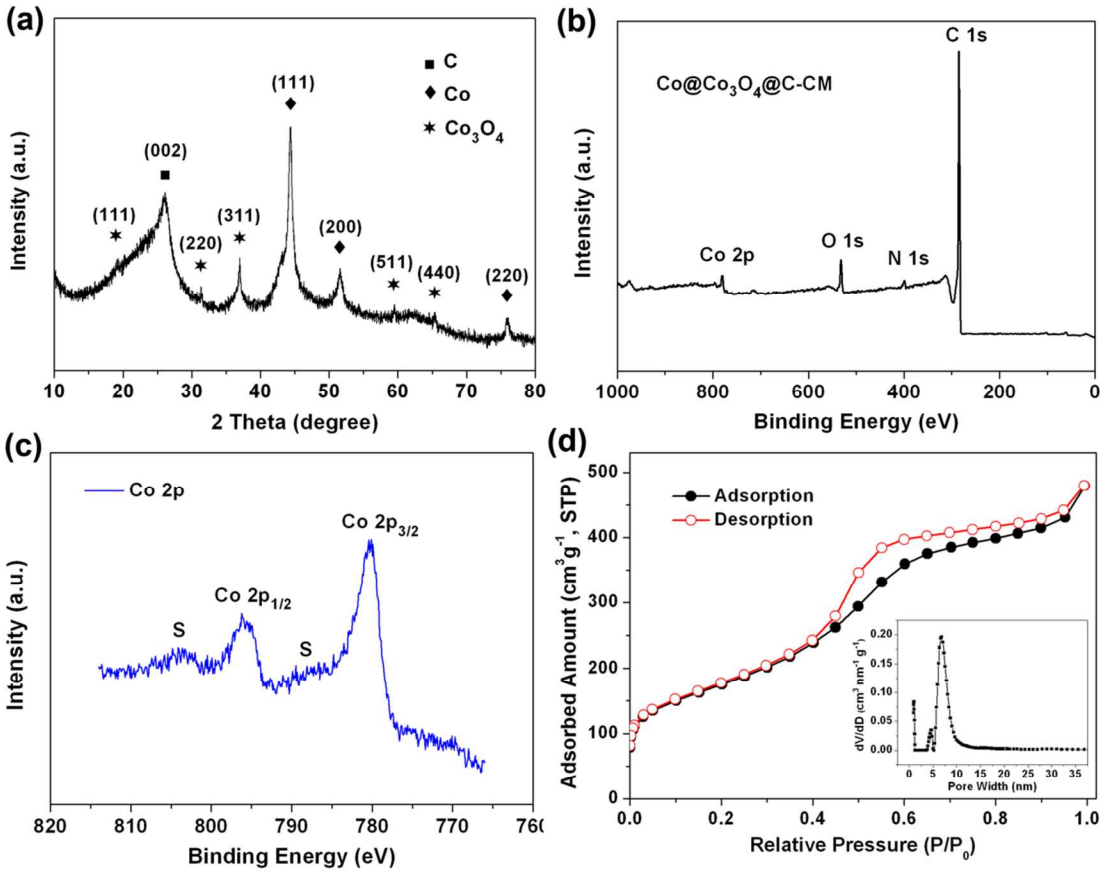

Fig.4 (a) PXRD pattern, (b) XPS full spectrum, (c) Co 2p XPS spectrum and (d) nitrogen sorption isotherms of the $Co@Co_3O_4@C$-CM composite. The inset in **4d** shows corresponding pore size distribution based on Quenched Solid Density Functional Theory (QSDFT) model using the adsorption branch.

The chemical composition of $Co@Co_3O_4@C$-CM was confirmed by PXRD and XPS. As shown in **Fig. 4a**, the PXRD pattern shows obvious C, Co and Co_3O_4 peaks. The relatively sharp carbon peak at 26.1° mainly comes from carbon shell that was formed under catalytic effect of the cobalt core at high temperature, similar to the formation process of CNT promoted by transition metal.[32] Thus, the catalysis of Co can promise the carbon shell with higher graphitization degree than individual CM (**Fig. S6**). After Co core was further oxidized in the air for 96 h, $Co_3O_4@C$-CM was obtained, confirmed by appearance of the typical Co_3O_4 peaks in PXRD pattern (**Fig. S7**). The full XPS spectrum of $Co@Co_3O_4@C$-CM reveals the presence of carbon, cobalt, nitrogen and oxygen species (**Fig. 4b**). The nitrogen actually comes from the decomposed benzimidazolate ligands, with a content of 1.72 at%. High-resolution XPS spectrum of the N peak shows pyridinic (398.9 eV), pyrrolic (400.4 eV) and oxidized (403.8 eV) nitrogen in the C shell (**Fig. S8**).[33,34] The regional Co 2p spectrum in **Fig. 4c** reveals a high energy band at 795.7 eV ($Co\ 2p_{1/2}$) and a low energy band at 780.3 eV ($Co\ 2p_{3/2}$), being in accordance with the report for Co_3O_4.[35,36] Moreover, the ~15eV energy difference between the two bands indicates the existence of both Co^{2+} and Co^{3+} species in the composite, which was further confirmed from the weak 2p satellite peaks in **Fig. 4c** (marked by S).[35]

$Co@Co_3O_4@C$-CM shows the Type IV isotherms (IUPAC definition) with a high Brunauer-Emmett-Teller (BET) surface area of 616 $m^2\ g^{-1}$ (**Fig. 4d**). The high nitrogen uptakes at the low relative pressure indicate the high microporosity, while the H1 hysteresis loop reveals the presence of cylindrical mesopores.[37] It's noteworthy that the pyrolyzed MOF displays the similar nitrogen sorption isotherms but with a different H4 hysteresis loop (**Fig. S9a**), representing the slits pores generated from plate-like particles' aggregation.[38] Furthermore, a quite wide pore size distribution ranging from micropores to mesopores is observed for $Co@Co_3O_4$-C (**Fig. S9b**). In contrast, $Co@Co_3O_4@C$-CM shows highly ordered mesopores centered at 7 nm and a small portion of micropores centered at 1 nm (**Fig. 4d**), similar to that of MOF-CM (**Fig. S10**). Combined with the above information from the shape of sorption isotherms, it is proposed that the mesopores actually come from CM and the micropores are in the

Cite this: DOI: 10.1039/c0xx00000x

www.rsc.org/xxxxxx

ARTICLE TYPE

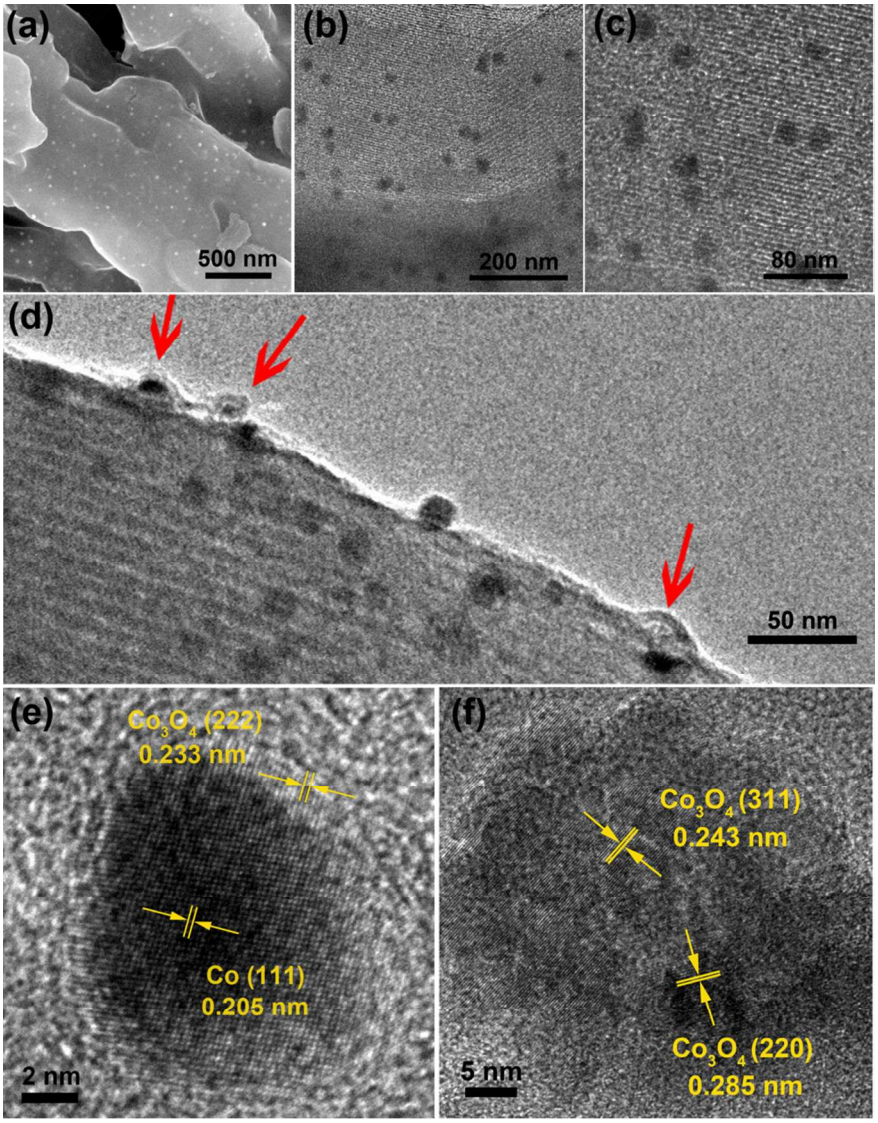

Fig. 5 (a) SEM and (b-d) TEM images of Co@Co_3O_4@C-CM. HRTEM images of (e) Co@Co_3O_4@C-CM and (f) Co_3O_4@C-CM.

carbon shell from Co@Co_3O_4@C NPs (**Fig. S11**). These results further indicate that the highly ordered structure of CM can be well maintained in Co@Co_3O_4@C-CM after the high-temperature treatment process, which is the key for enhancing the transport of oxygen and electrolyte onto the catalyst surface.

SEM images of Co@Co_3O_4@C-CM show that Co@Co_3O_4@C NPs are uniformly distributed and anchored on the outside walls of CM (**Fig. 5a** and **Fig. S12**). TEM images demonstrate that the highly dispersed Co@Co_3O_4@C NPs with the diameter of 15~30 nm are basically embedded inside CM (**Fig. 5b-d**, **Fig. S13**). Note that the size of Co@Co_3O_4@C is larger than the pore diameter of CM and Co@Co_3O_4@C NPs do not simply embed in the pore channels. Examples of NPs confined in order porous materials, like SBA-15, have been reported.[39] In those systems, the sizes of the NPs in SBA-15 were smaller than the pore diameter of SBA-15. This is because that SBA-15 possesses interconnected solid walls, which limits the size of the NPs between the walls (**Fig. S14**). However, the structure of porous host CM in this research is very different from that of SBA-15. The CM particle assembles from ordered arrays of carbon rods, and pores come from the leftover place between these carbon rods in the whole CM particle. Thus, the pores are three-dimensional interconnected. As depicted in **Fig. S15**, large cobalt particles from gradual aggregation of ultra-fine cobalt NPs on the carbon rods can locate in the CM particle by enwrapping several neighboring carbon rods. Moreover, Co@Co_3O_4 NPs are mainly covered by a graphene-sheet-like porous carbon shell (**Fig. 5d**). In order to further prove the existence of carbon shell,

Cite this: DOI: 10.1039/c0xx00000x

www.rsc.org/xxxxxx

ARTICLE TYPE

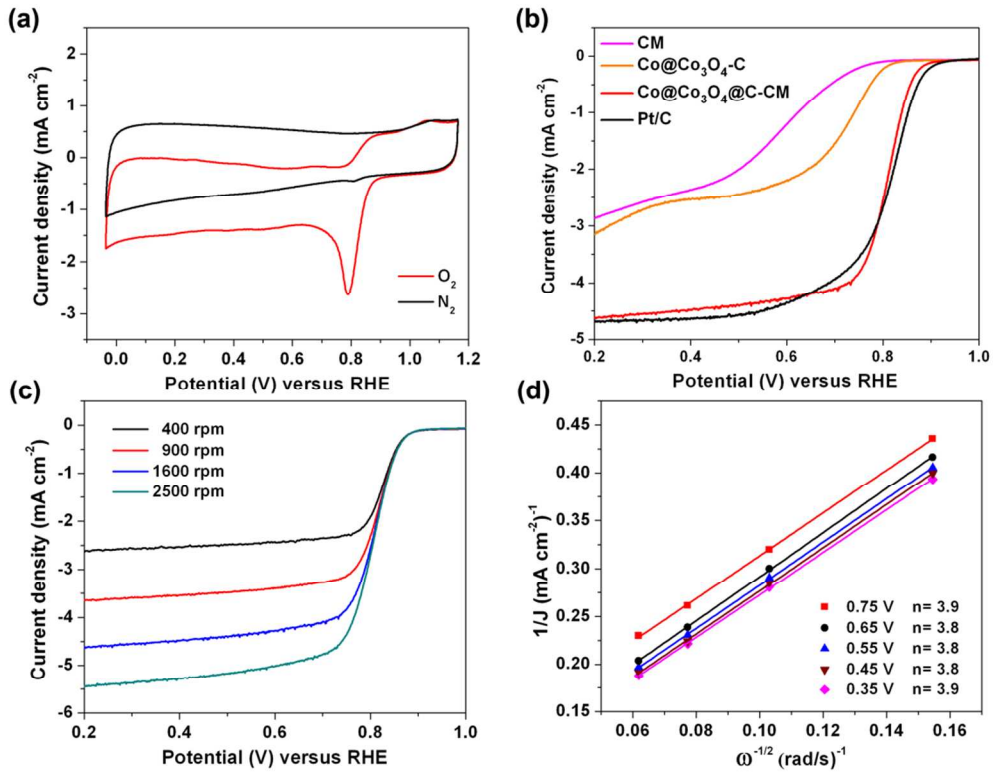

Fig. 6 (a) CVs of $Co@Co_3O_4$@C-CM at the scan rate of 50 mV s^{-1}. (b) ORR polarization curves of CM, $Co@Co_3O_4$-C, $Co@Co_3O_4$@C-CM and Pt/C (scan rate: 10 mV s^{-1}; rotation rate: 1600 rpm). (c) ORR polarization curves of $Co@Co_3O_4$@C-CM at various rotating rate (scan rate: 10 mV s^{-1}). (d) Koutechy-Levich plots of $Co@Co_3O_4$@C-CM at various potentials.

$Co@Co_3O_4$@C-CM was treated with strong acid to remove the $Co@Co_3O_4$ core (0.5 M H_2SO_4, 80 °C) (**Fig. S16**). As shown in **Fig. S17**, thin hollow carbon nanosphere is observed, providing direct evidence on the existence of carbon shell on the surface of $Co@Co_3O_4$ core. This conclusion can be further proved by observing a new peak at about 13 nm related to hollow carbon sphere in the pore size distributions of $Co@Co_3O_4$@C-CM after acid washing (**Fig. S18**). The introduction of CM is vital for the formation of novel $Co@Co_3O_4$@C NPs, verified by appearing the disordered structure of $Co@Co_3O_4$-C derived from pure MOF precursor (**Fig. S19**). For $Co@Co_3O_4$-C, consisting of very large particles, $Co@Co_3O_4$ NPs are embedded in the dense carbon particles generated from decomposed MOF ligands. While in the $Co@Co_3O_4$@C-CM composite, $Co@Co_3O_4$ NPs were well dispersed in open space due to the introduction of CM. The decomposed MOF ligands formed the carbon shell on $Co@Co_3O_4$ instead of large carbon particle. Thus, the active sites can be fully exposed and the mass transportation is easier in $Co@Co_3O_4$@C-CM. To explore the fine structure of $Co@Co_3O_4$@C-CM, HRTEM images were taken and showed in **Fig. 5e**. $Co@Co_3O_4$ NPs display a spherical morphology with singe-crystalline core and thin shell. The lattice fringe of the inner core is consistent with Co crystal structure and the layers outside the Co core are proved to be Co_3O_4 (**Fig. 5e**). In addition, HRTEM image from **Fig. 5f** and **Fig. S20** reveals that the Co core could be fully transformed into polycrystalline Co_3O_4 after complete oxidation, as proved by the appearance of well-defined (311) and (220) lattice fringe of Co_3O_4.

The ORR catalytic performance was first evaluated by CVs of different catalysts in 0.1 M KOH solution (**Fig. 6a** and **Fig. S21**). In N_2-saturated solution, all the catalysts deliver featureless CV curves. In contrast, they show the well-defined cathodic peaks for ORR in O_2-saturated 0.1 M KOH solution. $Co@Co_3O_4$@C-CM shows a pronounced cathodic peak for ORR at 0.79 V versus RHE, which is more positive than that of pure MOF derived catalyst and CM (**Fig. S21**). The ORR polarization curves of $Co@Co_3O_4$@C-CM, $Co@Co_3O_4$-C, CM and Pt/C catalyst are showed in **Fig. 6b**. It is found that $Co@Co_3O_4$-C prepared directly from pure MOF crystals has the onset potential of 0.85 V and half-wave potential of 0.70 V. Surprisedly, $Co@Co_3O_4$@C-CM shows much higher activity for ORR with an onset potential of 0.93 V and half-wave potential of 0.81 V, which is very close to that of commercial Pt/C catalyst. From the comparison of the ORR performance of $Co@Co_3O_4$-C and $Co@Co_3O_4$@C-CM, the benefit from CM addition in MOF-derived catalyst can be revealed. CM provides three-dimensional interconnected pore structure, in which MOF derived ORR active $Co@Co_3O_4$@C NPs are fully exposed to oxygen and electrolyte. The high values

Cite this: DOI: 10.1039/c0xx00000x

www.rsc.org/xxxxxx

ARTICLE TYPE

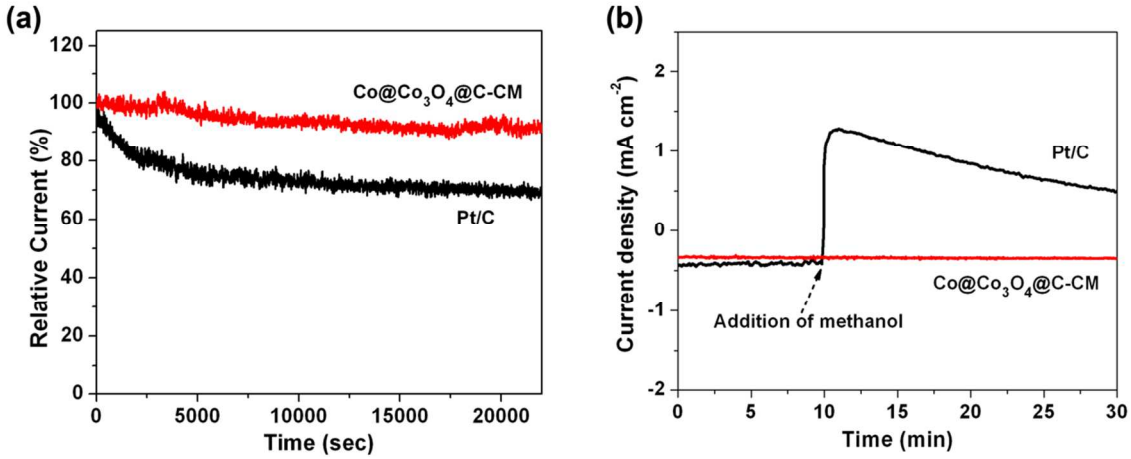

Fig. 7 (a) Chronoamperometric responses of $Co@Co_3O_4@C$-CM and Pt/C at 0.75 V. (b) Chronoamperometric responses of $Co@Co_3O_4@C$-CM and Pt/C upon addition of 3 M methanol into O_2-saturated 0.1 M KOH at 0.75 V. Note that the loading amount of all catalysts is 0.1 mg cm^{-2}.

of $Co@Co_3O_4@C$-CM rank it among the best performed non-precious metal catalysts under the identical loading amount.[5,29] Moreover, the limit current density of $Co@Co_3O_4@C$-CM is much higher than that of $Co@Co_3O_4$-C or CM, and very close to that of the Pt/C catalyst. In the potential range of 0.6-0.8 V, $Co@Co_3O_4@C$-CM even shows steeper polarization curve and higher current density than commercial Pt/C, implying the very high ORR activity of present $Co@Co_3O_4@C$-CM.

The polarization curves at various rotating rates and corresponding Koutechy-Levich plots of $Co@Co_3O_4@C$-CM were collected and calculated, as shown in **Fig. 6c**,**d**. A good linearity of the plots and near parallelism of the fitting lines at various potentials were observed, suggesting the reactions on $Co@Co_3O_4@C$-CM are first-order over the potential range. As one of the important factors in evaluation of ORR catalysts, the preferred electron transfer number (n) is 4. Calculated from Koutechy-Levich equation, the electron transfer number on $Co@Co_3O_4@C$-CM ranges from 3.8 to 3.9, which is also very close to the value obtained from RRDE curve (**Fig. S22**), implying that our designed catalyst favors the 4-electron ORR process.

Stabilities of the catalysts were evaluated using chronoamperometric measurement. The current-time (i-t) curve shows a high stability for $Co@Co_3O_4@C$-CM (**Fig.7a**). It delivers a slight current loss with high retention of more than 90 % after 25000 s. In contrast, Pt/C catalyst suffers a rapid current loss with only 68 % retention. Furthermore, the tolerance toward methanol of $Co@Co_3O_4@C$-CM and commercial Pt/C were determined upon addition of 3 M methanol into 0.1 M KOH electrolyte using i-t technique. **Fig. 7b** shows no obvious change in the current density for $Co@Co_3O_4@C$-CM after the addition of methanol. However, the Pt/C catalyst shows a sharp jump in i-t curve due to the methanol oxidation reaction. These results suggest that $Co@Co_3O_4@C$-CM has much better catalytic selectivity toward ORR than the commercial Pt/C catalyst.

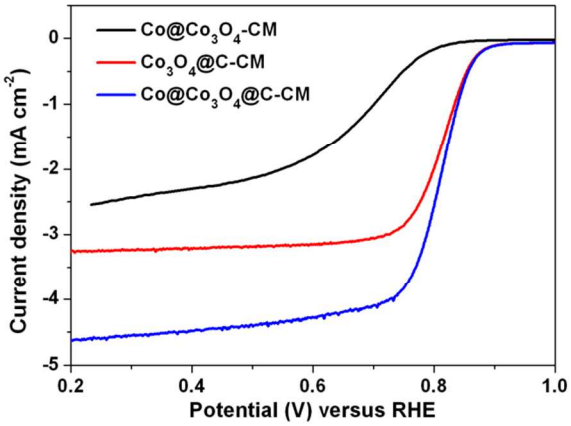

Fig. 8 ORR polarization curves of $Co@Co_3O_4$-CM, $Co_3O_4@C$-CM and $Co@Co_3O_4@C$-CM (scan rate: 10 mV s^{-1}; rotation rate: 1600 rpm).

In order to better understand the role of Co core and carbon shell in the resulting $Co@Co_3O_4@C$-CM, the ORR activities of $Co_3O_4@C$-CM and $Co@Co_3O_4$-CM were conducted, and shown in **Fig. 8**. (i) Considering that the Co core in $Co@Co_3O_4@C$-CM may affect the catalytic activity, we first compared the ORR activities of partially oxidized $Co@Co_3O_4@C$-CM and full oxidized $Co_3O_4@C$-CM (**Fig. 8**). $Co_3O_4@C$-CM shows slightly lower onset potential with much lower current density than $Co@Co_3O_4@C$-CM, indicating that the Co as a core can promote the ORR process. Given that the Co cores were covered by Co_3O_4 shells, their direct contact with oxygen and electrolyte will be not easy. Herein, Co cores might affect the properties of the surrounding shells by modifying the electron density, as shown in iron encapsulated within carbon nanotube.[40] However, further theoretical investigation is needed to better understand such interaction. (ii) The graphene-sheet-like carbon shells generated

from decomposed benzimidazolate ligands is critical for the fine structure and good ORR performance of Co@Co_3O_4@C-CM. Benzimidazolate is an aromatic precursor that has been proved to be effective to generate graphitic carbon with improved catalytic activity.[32,41] Moreover, the carbon shells derived from benzimidazolate were nitrogen-doped, which can also partly contribute to the ORR activity. Our result indeed shows that C-CM sample, prepared by acid etching of Co@Co_3O_4@C-CM, displayed remarkable improvement for ORR relative to pure CM **(Fig. S23)**. To verify the deeper effect from the carbon shell, Co@Co_3O_4-CM without carbon shell on Co@Co_3O_4 was prepared *via* a conventional wet-impregnation method. It showed much lower catalytic activity compared with Co@Co_3O_4@C-CM (**Fig. 8** and **Fig. S24**). The onset potential of Co@Co_3O_4-CM was nearly 70 mV lower than that of Co@Co_3O_4@C-CM. TEM image reveals that the metal NPs without protection from the carbon shell tend to agglomerate during heat treatment and form very large particles in Co@Co_3O_4-CM (**Fig. S25**), which decreases the exposed catalytic surface and thus the ORR performance. Although NPs in the Co@Co_3O_4@C-CM composite were obtained from higher temperature, they had smaller size and were well-dispersed due to the protection from the carbon shells. Moreover, the carbon shells had close contacts with Co@Co_3O_4 NPs, which could be helpful in delivering electron from the carbon support to Co@Co_3O_4 NPs during ORR process. All of them, put together, illustrate the role of the carbon shell from MOF towards in lowering ORR overpotential and increasing current density in the Co@Co_3O_4@C-CM catalyst.

The higher ORR activity of Co@Co_3O_4@C-CM than Co@Co_3O_4-C nanocatalyst derived from pure MOF crystals can mainly be ascribed to the following aspects. The open highly ordered mesoporous structure of Co@Co_3O_4@C-CM provided excellent mass-transport property. ORR usually involves a heterogeneous process at triple-phase boundary, requiring the contacts of oxygen, electrolyte and the solid catalyst. Faster exchange of the gas and electrolyte at the catalyst surface could accelerate the ORR process. As depicted in **Fig. 1**, Co@Co_3O_4-C possessed the dense particulate structure with disordered slit pores. Therefore, it was difficult to achieve the good mobility of oxygen and electrolyte. Moreover, a large portion of the ORR active NPs were embedded in the dense catalyst particles and only a small part on the outside layers played the role in ORR catalysis. In contrast, Co@Co_3O_4@C-CM had the ideal open structure for ORR. The Co@Co_3O_4@C sites were uniformly encapsulated into the highly porous CM, ensuring full contacts with gas and electrolyte. Meanwhile, the transportation of these species in Co@Co_3O_4@C-CM was remarkably enhanced due to the reduced overall diffusion resistance.

Conclusions

In summary, a novel Co@Co_3O_4@C-CM core@bishell composite structure was successfully constructed through first confined growth of MOF on ordered CM, and then sequential heat treatment of the as-prepared MOF-CM precursor in argon and air. Combined with the porous matrix possessing interconnected ordered channels, good activity of Co@Co_3O_4@C NPs and strong coupling/interaction between NPs and CM, the Co@Co_3O_4@C-CM catalyst shows excellent ORR activity. It exhibits a high ORR onset potential of 0.93 V and half-wave potential of 0.81 V, ranking it among the best performed non-precious metal catalysts. It also shows superior stability to that of commercial Pt/C catalyst, and good tolerance to methanol cross-over effect. This work provides a general method to construct novel metal@metal-oxide@carbon core@bishell nanostructure and opens new avenue for the application of MOFs in high-efficiency electrocatalysts. Due to various metal and organic ligand combinations to fabricate MOFs, more core@bishell nanostructures with various metal centers and heteroatoms like N, P, S doped carbon shells could be designed and expected to be more active for ORR.

Acknowledgements

The authors thank Dr. A. Burrell for valuable discussions and careful revision of the manuscript. This work was supported by National Natural Science Foundation of China 51322205 and 21371014, New Star Program of Beijing Committee of Science and Technology (2012004), the Ministry of education program for New Century Excellent Talents of China (NCET-11-0027). The authors thank the reviewers for their constructive suggestions.

Notes and references

[a]*College of Engineering, Peking University, Beijing 100871, China; E-mail: rzou@pku.edu.cn*
[b]*Physical Chemistry and Applied Spectroscopy, Los Alamos National Laboratory, Los Alamos, NM 87545, USA; E-mail: shaojun.guo.nano@gmail.com*

† Electronic Supplementary Information (ESI) available: PXRD, TEM, XPS, nitrogen sorption and CV tests. See DOI: 10.1039/b000000x/

1 A. A. Gewirth, M. S. Thorum, *Inorg. Chem.* 2010, **49**, 3557.
2 H. A. Gasteiger, N. M. Marković, *Science* 2009, **324**, 48.
3 H. A. Gasteiger, S. S. Kocha, B. Sompalli, F. T. Wagner, *Applied Catalysis B: Environmental* 2005, **56**, 9.
4 G. Wu, P. Zelenay, *Acc. Chem. Res*. 2013, **46**, 1878.
5 Y. Zheng, Y. Jiao, M. Jaroniec, Y. G. Jin, S. Z. Qiao, *Small* 2012, **8**, 3550.
6 S. Gupta, D. Tryk, I. Bae, W. Aldred, E. Yeager, *J. Appl. Electrochem.* 1989, **19**, 19.
7 M. Lefèvre, E. Proietti, F. Jaouen, J. P. Dodelet, *Science* 2009, **324**, 71.
8 G. Wu, K. L. More, C. M. Johnston, P. Zelenay, *Science* 2011, **332**, 443.
9 J. P. Dodelet, in N4-Macrocyclic Metal Complexes (Eds.: J. H. Zagal, F. Bedioui, J. P. Dodelet), Springer, New York, 2006, pp. 83-147.
10 J. L. C. Rowsell, O. M. Yaghi, *Microporous Mesoporous Mater.* 2004, **73**, 3.
11 H. H. Wu, Q. H. Gong, D. H. Olson, J. Li, *Chem. Rev.* 2012, **112**, 836.
12 R. E. Morris, P. S. Wheatley, *Angew. Chem. Int. Ed.* 2008, **47**, 4966.
13 S. L. Li, Q. Xu, *Energy Environ. Sci.* 2013, **6**, 1656.
14 B. Liu, H. Shioyama, T. Akita, Q. Xu, *J. Am. Chem. Soc.* 2008, **130**, 5390.
15 M. Hu, J. Reboul, S. Furukawa, N. L. Torad, Q. M. Ji,P. Srinivasu, K. Ariga, S.Kitagawa, Y. Yamauchi, *J. Am.Chem. Soc.* 2012, **134**, 2864.
16 W. Xia, B. Qiu, D. G. Xia, R. Q. Zou, *Sci. Rep.* 2013, **3**, 1935.
17 S. Q. Ma, G. A. Goenaga, A. V. Call, D. J. Liu, *Chem. Eur. J.* 2011, **17**, 2063.
18 E. Proietti, F. Jaouen, M. Lefèvre, N. Larouche, J. Tian,J. Herranz, J. P. Dodelet, *Nat. Commun.* 2011, **2**, 416.
19 P. Zhang, F. Sun, Z. H. Xiang, Z. G. Shen, J. Yun, D. P. Cao, *Energy Environ. Sci.* 2014, **7**, 442.
20 T. Y. Ma, S. Dai, M. Jaroniec, S. Z. Qiao, *J. Am. Chem. Soc.* 2014, **136**, 13925.

21 W. Xia, J. H. Zhu, W. H. Guo, L. An, D. G. Xia, R. Q. Zou, *J. Mater. Chem. A* 2014, **2**, 11606.

22 Y. Y. Liang, Y. G. Li, H. L. Wang, J. G. Zhou, J. Wang, T. Regier, H. J. Dai, *Nat. Mater.* 2011, **10**, 780.

23 Y. Y. Liang, Y. G. Li, H. L. Wang, H. J. Dai, *J. Am. Chem. Soc.* 2013, **135**, 2013.

24 K. S. Park, Z. Ni, A. P. Côté, J. Y. Choi, R. D. Huang, F. J. Uribe-Romo, H. K. Chae, M. O'Keeffe, O. M. Yaghi, *Proc. Natl. Acad. Sci. USA*. 2006, **103**, 10186.

25 S. Jun, S. H. Joo, R. Ryoo, M. Kruk, M. Jaroniec, Z. Liu, T. Ohsuna, O. Terasaki, *J. Am. Chem. Soc.* 2000, **122**,10712.

26 A. Vinu, K. Z. Hossian, P. Srinivasu, M. Miyahara, S. Anandan, N. Gokulakrishnan, T. Mori, K. Ariga, V. V. Balasubramanian, *J. Mater. Chem.* 2007, **17**, 1819.

27 H. J. Lee, W. Cho, M. Oh, *Chem. Commun.* 2012, **48**, 221.

28 S. Sorribas, B. Zornoza, C. Téllez, J. Coronas, *Chem. Commun.* 2012, **48**, 9388.

29 S. J. Guo, S. Zhang, L. H. Wu, S. H. Sun, *Angew. Chem. Int. Ed.* 2012, **51**, 11770.

30 A. Navrotsky, C. C. Ma, K. Lilova, N. Birkner, *Science* 2010,**330**, 199.

31 D. H. Ha, L. M. Moreau, S. Honrao, R. G. Hennig, R. D. Robinson, *J. Phys. Chem. C* 2013,**117**, 14303.

32 G. Wu, N. H. Mack, W. Gao, S. G. Ma, R. Q. Zhong, J. T. Han, J. K. Baldwin, P. Zelenay, *ACS Nano* 2012, **6**, 9764.

33 T. Sharifi, G. Z. Hu, X. E. Jia, T. Wågberg, *ACS Nano* 2012, **6**, 8904.

34 Z. H. Sheng, L. Shao, J. J. Chen, W. J. Bao, F. B. Wang, X. H. Xia, *ACS Nano* 2011, **5**, 4350.

35 L. Fu, Z. M. Liu, Y. Q. Liu, B. X. Han, P. Hu, L. C. Cao, D. B. Zhu, *Adv. Mater.* 2005, **17**, 217.

36 J. W. Xiao, Q. Kuang, S. H. Yang, F. Xiao, S. Wang, Lin. Guo, *Sci. Rep.* 2013, **3**, 2300.

37 N. Reichhardt, T. Kjellman, M. Sakeye, F. Paulsen, J. -H. Smått. M. Lindén, V. Alfredsson, *Chem. Mater.* 2011, **23**, 3400.

38 C. Lastoskie, K. E. Gubbins, N. Quirke, *Langmuir* 1993, **9**, 2693.

39 F. Gao, Q. Y. Lu, X. Y. Liu, Y. S. Yan, D. Y. Zhao, *Nano Lett.* 2001, **1**, 743.

40 D. H. Deng, L. Yu, X. Q. Chen, G. X. Wang, L. Jin, X. L. Pan, J. Deng, G. Q. Sun, X. H. Bao, *Angew. Chem. Int. Ed.* 2013, **52**, 371.

41 C. H. Kim, D. K. Lee, T. J. Pinnavaia, *Langmuir* 2004, **20**, 5157.

TOC

MOF-derived $Co@Co_3O_4@C$ core@bishell nanoparticles encapsulated into a highly ordered porous carbon matrix show very high catalytic activity and stability toward oxygen reduction reaction.